# DIGITAL ACCESS TO SCHOLARSHIP AT HARVARD

# Demon-like Algorithmic Quantum Cooling and Its Realization with Quantum Optics

*(Article begins on next page)*

# Demon-like Algorithmic Quantum Cooling and its Realization with Quantum Optics

Jin-Shi Xu,[1, *] Man-Hong Yung,[2, *] Xiao-Ye Xu,[1] Sergio Boixo,[2] Zheng-Wei Zhou,[1]
Chuan-Feng Li,[1, †] Alán Aspuru-Guzik,[2, ‡] and Guang-Can Guo[1]

[1]*Key Laboratory of Quantum Information, University of Science and Technology of China,
CAS, Hefei, 230026, People's Republic of China*
[2]*Department of Chemistry and Chemical Biology,
Harvard University, Cambridge MA, 02138, USA*
(Dated: August 13, 2012)

**The simulation of low-temperature properties of many-body systems remains one of the major challenges in theoretical [1–3] and experimental [4–6] quantum information science. We present, and demonstrate experimentally, a universal cooling method which is applicable to any physical system that can be simulated by a quantum computer [7–9]. This method allows us to distill and eliminate hot components of quantum states, i.e., a quantum Maxwell's demon [10]. The experimental implementation is realized with a quantum-optical network, and the results are in full agreement with theoretical predictions (with fidelity higher than 0.978). These results open a new path for simulating low-temperature properties of physical and chemical systems that are intractable with classical methods.**

From quantum field theories [1] to high-Tc superconductivity [2] and chemical reactions [3], quantum simulation [7–9] provides a unique opportunity for both theorists and experimentalists to explore a domain of science that goes beyond the applicability of any known classical computing method. Modern low-temperature physics has advanced primarily due to the development of efficient cooling methods [11, 12]. The same is also true for quantum information science. Physical cooling can drive quantum states towards the physical ground states, which are pure states. However, in the context of quantum simulation, pure states are not necessarily "cooler" than mixed states. For example, pure states with an equal superposition of all eigenstates correspond to infinite-temperature states [13, 14]. In order to achieve cooling for quantum simulation, in general, one not only needs to employ physical cooling to avoid decoherence [15], but also be able to prepare states that have low entropy in the basis of the eigenstates of the Hamiltonian of the system being simulated.

An attractive approach for achieving cooling for spins (or qubits) is the heat-bath algorithmic cooling (HBAC) method [16]. The main idea of HBAC is to reduce the entropy of spin systems by unevenly distributing more entropy to one of the spins that can release the excess entropy to a heat bath through thermalization. The feasibility of HBAC has been demonstrated experimentally with NMR technology [4]. However, HBAC is not a uni-
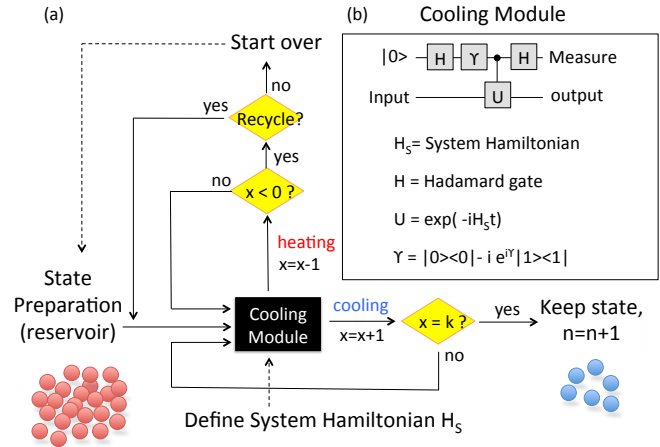


FIG. 1: (Color online). Overview of the cooling method. (a) Logic diagram of the feedback cooling system. The cooling module produces two outcomes, correlated with heating and cooling. The measurement result can be mapped into the position $x$ of a 1D random walker; when the walker goes beyond its starting position $x = 0$ to the negative position $x = -1$, the particle is either rejected or recycled. (b) The quantum circuit diagram of the cooling module. It includes a controlled evolution for time $t$ and an energy bias parameter $\gamma$ for optimizing the performance.

versal method for cooling quantum many-body systems; it is primarily employed for preparing polarized spins as initial states, or ancilla qubits, for quantum computation. Furthermore, the temperature of the environment imposes a fundamental limit for the cooling performance [17].

A more general approach [18, 19] for quantum cooling is to engineer a dissipative open-system dynamics to drive quantum states to the ground states of the simulated systems. This dissipative open-system (DOS) approach relaxes two criteria in the standard circuit model [20] for quantum information processing, namely specific initial-state preparation and full-unitary gate decomposition. As the underlying dynamics is based on Lindblad master equations, this approach is shown to be robust [21] against simulation errors. A proof-of-principle demonstration has been experimentally performed using trapped ions [5]. Despite the advantages the DOS ap-
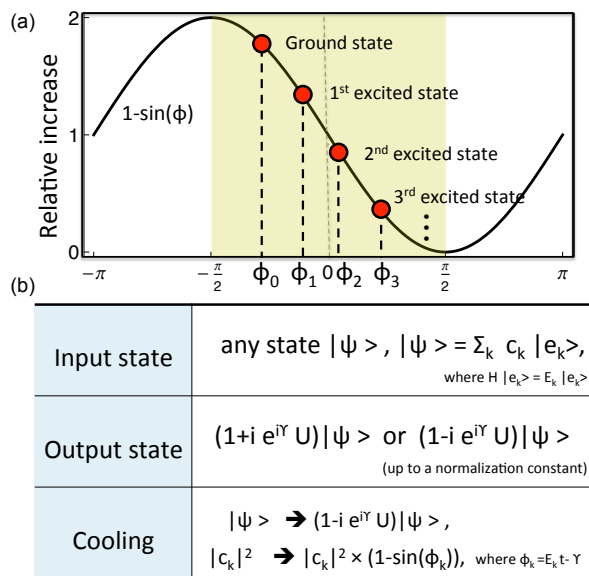
FIG. 2: (Color online). Basic principle of the cooling method. (a) The relative change in the population of the output state post-conditioned with a "cooling" measurement result depends on the eigenenergy $E_k$: the lower the energy, the higher the gain. Details are summarized in (b). (see also Eq. 1 and method summary).

proach can provide, the range of application of it is limited; practically, it is restricted to a class of system involving the so-called frustration-free Hamiltonians [19], where the ground state should simultaneously minimize all local terms in the Hamiltonian. This condition is not satisfied by the majority of physical Hamiltonians.

To overcome the challenges, in this work, we present a universal cooling method applicable to cooling any physical system that can be simulated by a quantum computer. Our method shares some features in the HBAC and the DOS approach, but does not suffer from the limitations of them. Essentially, we replace the requirement of the existence of a heat bath in HBAC by an ensemble of quantum states; thermalization is replaced by swapping with one of the states in the ensemble. As evident by our numerical analysis (see [22]), our method does not suffer from similar restrictions in HBAC for cooling spin-1/2 particles [17]. Furthermore, we adopted a feedback approach to result in an effective quantum operation for achieving cooling for quantum simulation. In DOS, each of the quantum jump operators encodes only partial information of the Hamiltonian to be simulated [18, 19]; in our case, the jump operators contain full information about the Hamiltonian. This property makes our cooling method universally applicable to any physical Hamiltonian.

To be more specific, for any given Hamiltonian $H_s$ and any input state, pure state $|\psi_{in}\rangle$ or mixed state $\rho_{in}$, the

method guarantees that the energy $E \equiv Tr\left(H_s \rho_{out}\right)$ of output state $\rho_{out}$ is less than (or equal to) that of the input state. Importantly, compared with DOS, our method does not increase the qubit resource required for cooling; other than the system qubits, it requires only one extra ancilla qubit, which is the same as in the DOS method. This not only significantly reduces computational resources but also makes the method more robust against noise and errors [21]. Therefore, our cooling method is as realizable as DOS with currently available technologies; we experimentally performed a proof-of-principle demonstration with quantum-optics, which is reported below.

The core component of the method is the 'cooling module' formed by a simple quantum circuit shown in Fig. 1. It consists of an ancilla qubit initialized into the $|0\rangle$ state, a pair of Hadamard gates $\mathsf{H} = \left(1/\sqrt{2}\right)\left[(|0\rangle + |1\rangle)\langle 0| + (|0\rangle - |1\rangle)\langle 1|\right]$, a local phase gate $\gamma = |0\rangle\langle 0| - ie^{i\gamma}|1\rangle\langle 1|$, and a controlled unitary operation $U = \exp\left(-iH_s t\right)$, where $H_s$ is the Hamiltonian to be simulated. We note that the unitary time evolution for most of the physical Hamiltonians can be efficiently simulated with a quantum computer [7]. For any input state $|\psi_{in}\rangle$, the quantum circuit produces the following state [22]:

$$\Lambda_- |\psi_{in}\rangle |0\rangle + \Lambda_+ |\psi_{in}\rangle |1\rangle \quad , \quad (1)$$

where $\Lambda_\pm \equiv \left(I \pm ie^{i\gamma}U\right)/2$. Next, the ancilla qubit is measured in the computational basis $\{|0\rangle, |1\rangle\}$. Similar to the working mechanism of DOS [5, 18, 19, 21], the non-unitary operators $\Lambda_\pm$ play similar roles as quantum jump operators for describing the state evolution. Moreover, we found that (see [22]) the energy of the resulting state $\Lambda_- |\psi_{in}\rangle$ $(\Lambda_+ |\psi_{in}\rangle)$, after nomalization of the vector norms, is lower (higher) than that of the input state $|\psi_{in}\rangle$. Consequently, the cooling module probabilistically projects any input state $|\psi_{in}\rangle$ (or $\rho_{in}$ for mixed states), into either a higher-energy state $\Lambda_+ |\psi_{in}\rangle$ (ancilla output $|1\rangle$) or a lower-energy state $\Lambda_- |\psi_{in}\rangle$ (ancilla output $|0\rangle$), with respect to the Hamiltonian $H_s$ being simulated (see Fig. 2a and 2b, and [22] for a step-by-step derivation). Eq. 1 represents the key element in our cooling method.

In the next step, the resulting state $\Lambda_\pm |\psi_{in}\rangle$ will either be sent to another cooling module for further cooling, or recycled/rejected (see method), depending on the measurement outcome. We formulated this procedure as a feedback-control loop as depicted in Fig. 1a. As governed by the laws of quantum mechanics, the measurement outcomes of the ancilla qubit are intrinsically random. We model the cooling process as a 1D random walk by keeping track of the sequence of the measurement outcomes. A net cooling effect can be achieved by implementing the feedback system that employs the following mapping: consider a random walker starts at position $x = 0$. If the measurement outcome is $|0\rangle$, then $x$ is increased by 1, and decreased by 1 for $|1\rangle$. When
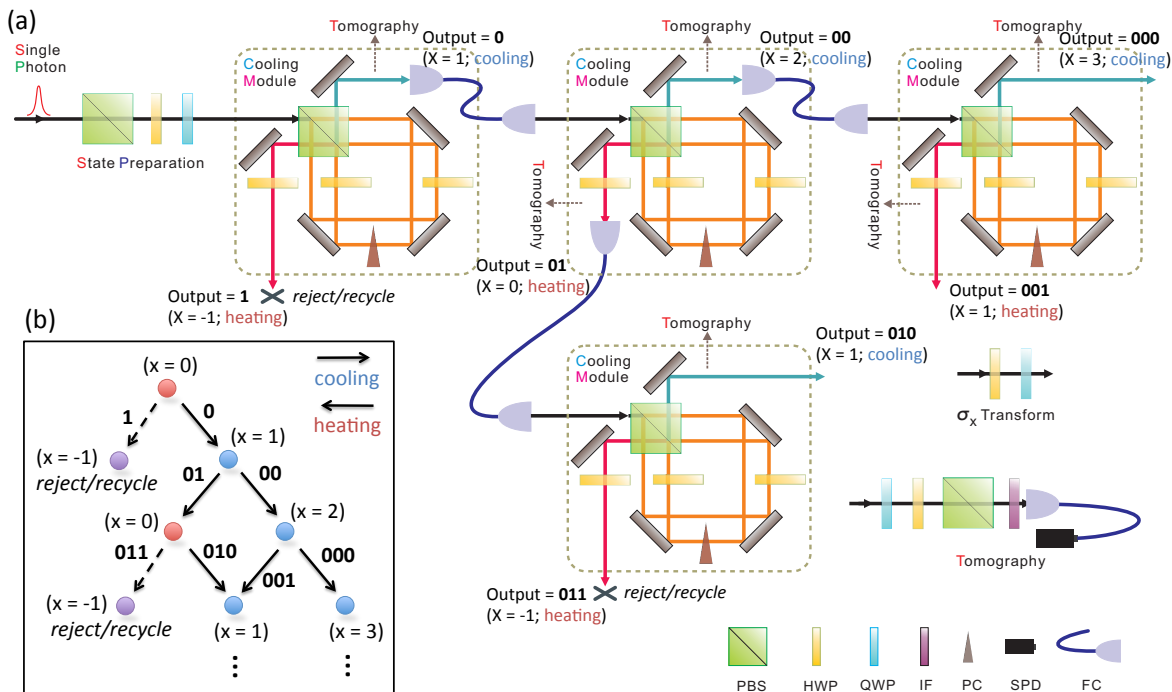
FIG. 3: (Color online). Experimental details. (a) The input photon state is prepared by a polarization beam splitter (PBS), a half-wave plate (HWP) and a quarter-wave plate (QWP). The cooling module is a polarization-dependent Sagnac interferometer. Split by the PBS, the horizontal and vertical components of a polarized photon propagate in opposite paths within the interferometer. Two HWPs operate on the corresponding polarization components. The quartz plate compensator (PC) is used to compensate for the relative phase in the interferometer. These elements simulate the system Hamiltonian. Both paths are then recombined on the same PBS. The photons at output ports 0 and 1 represent the cases of cooling and heating, respectively. The photon proceeds to the next cooling module depending on the value of the position $x$ of the random walker. The final quantum state is reconstructed using quantum state tomography, with the measurement bases defined by a QWP, HWP and PBS. The photon is detected by a single photon detector (SPD) equipped with a 3 nm interference filter (IF). When the simulated Hamiltonian is $\sigma_x$, a HWP with an angle of $22.5°$ and a tiltable QWP with an horizontal angle implement the $\sigma_x$ transformation at the input and output ports. (b) Sketch of the random walker evolution.

the random walker goes beyond the origin to the negative side ($x < 0$), it is either discarded ("evaporative" strategy) or recycled ( "recycling" strategy) where the system is reset to the the initial state $|\psi_{in}\rangle$ (see [22] for more details). In implementing the evaporative strategy, we assumed an initial ensemble of identical states (red particles in Fig. 1a). When the random walker position is set to $x = -1$, then the system is rejected, and we restart the experiment with another member in the ensemble. Just like ordinary evaporative cooling, this results in a decrease of overall energy but at a cost of loss of particles (blue particles in Fig. 1a). For the recycling strategy, it is applicable to a single system. We assume the same initial state can be prepared efficiently. When the random walker position is set to $x = -1$, we simply reset the quantum state of the system to the same initial state. For $x \neq 1$, both strategies work in exactly the same way.

We note that the recycling strategy resembles the way of releasing entropy through thermalization in HBAC.

The main difference is that we correlate high-entropy states with the position ($x < 0$) of the random walker instead of including a pre-assigned qubit as heat sink in HBAC. The performance and trade-off of the two strategies will be compared and explained in the experimental section. In both cases, the random walker undergoes a diffusion toward the $x > 0$ direction (see Fig. 3b). A detailed scaling analysis with Monte Carlo simulation is provided in [22].

In fact, the cooling module is effectively a realization of the thought experiment of Maxwell's demon [10]: an intelligent being who is able to separate hot and cool particles, which decreases the system's entropy without any work being done on it. In our setup, ancilla qubits are constantly refreshed, and they therefore serve as an entropy sink. Each measurement outcome of the cooling module reveals partial information about the eigenstates of $H_s$. If we repeatedly apply the cooling module to the same system, the process is asymptotically close to a quantum non-demolition measurement [23] in

the eigenstate basis of $H_s$ (see [22] for details). In other words, entropy (in the energy basis) is removed from the system by measurements, instead of employing an external heat bath as in the heat-bath algorithmic cooling method [4, 16].

Below, we report a proof-of-principle demonstration of the quantum cooling method with an all-optical setup (see e.g. [24] for a recent review of photonic quantum simulation). We built a network of optical elements to connect four cooling modules (see Fig. 3a) to implement a multiple-step quantum cooling. This setup is specifically designed for cooling the polarization degrees of freedom of a single photon (see [22] for requirements for a scalable implementation). The simulated quantum system has only two levels, i.e., a qubit. To illustrate the flexibility of the setup, two different Hamiltonians $H_s$ were simulated, namely Pauli's matrices $\sigma_z = \begin{pmatrix} 1 & 0 \\ 0 & -1 \end{pmatrix}$ and $\sigma_x = \begin{pmatrix} 0 & 1 \\ 1 & 0 \end{pmatrix}$. We emphasize that although the Hamiltonians to be simulated are relatively simple, the ground states are not assumed to be known. The other specifications of the simulation are as follows: the logical Hilbert space of the system was encoded in the photonic polarization $\{|H\rangle, |V\rangle\}$ from a single photon source, where $|H\rangle$ and $|V\rangle$ respectively refer to the horizontally and vertically polarized state of a photon. The which-path degree of freedom $\{|0\rangle, |1\rangle\}$ was employed as the ancilla qubit in the quantum circuit (see Eq. 1). The evolution operator $U(t) = \exp(-iH_s t)$ was simulated for a fixed period of $t = \pi/2$. An energy offset, defined as

$$\theta \equiv \gamma + \pi/2 \quad , \qquad (2)$$

where $\gamma$ is defined in Fig. 1b, was used as an adjustable parameter for characterizing the cooling efficiency. The goal of the experiment is to minimize the mean energy $\langle \sigma_z \rangle$ (or $\langle \sigma_x \rangle$) for any given initial state.

Each of the cooling modules were realized by a polarization-dependent Sagnac interferometer (circled by dotted lines in Fig. 3a); similar, but not identical, structures [25, 26] have been used for tasks related to quantum information processing. The quantum state $|\psi_{in}\rangle$ of the incident photon was prepared by a series of optical elements shown in Fig. 3a. The optical components inside the cooling module result in quantum logical operations [27] which are equivalent to that described in Eq. 1 (see [22] for details). The photon leaving from one of the two output ports of the cooling module is in a superposition state (see Eq. 1) containing both outcomes of heating $|1\rangle$ (red arrow) and cooling $|0\rangle$ (blue arrow). Subsequent detection of the two paths corresponds to a projective measurement in the ancilla qubit space, and will result in one of the two output states $\Lambda_\pm |\psi_{in}\rangle$.

For the first cooling module, a single step of cooling is achieved if the measurement outcome is $|0\rangle$. To further extract energy from the system, multiple steps of cooling events are needed. To proceed, four identical cooling modules are connected by optical fibers. The network
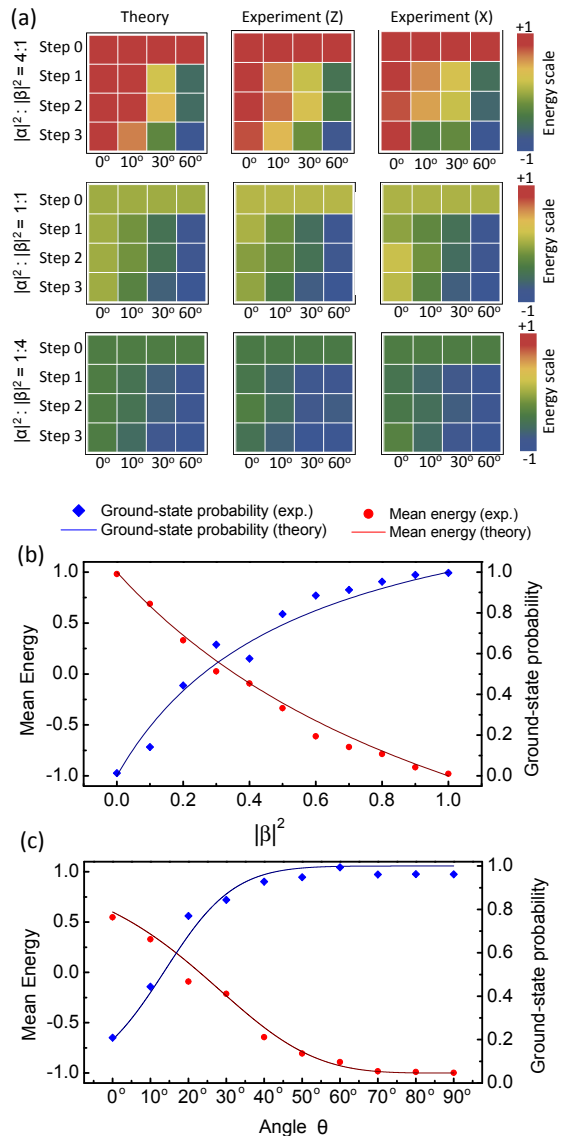


FIG. 4: (Color online). Experimental results. (a) Mean energies for 3 cooling steps of the evaporative (non-recycling) strategy for different $\theta$. Different maps correspond to theory and experiment for Hamiltonians $\sigma_z$ (Z) and $\sigma_x$ (X), and different initial states (step 0). (b) Theoretical and experimental mean energy and ground state probability after the 3rd cooling step as a function of the initial ground-state overlap $|\beta|^2$. The evaporative strategy simulated the Hamiltonian $\sigma_z$ with energy bias angle $\theta = 10°$. (c) Theoretical and experimental mean energy and ground state probability after the 3rd cooling step as a function of $\theta$. The initial input state was $(2/\sqrt{5})|e\rangle + (1/\sqrt{5})|g\rangle$ ($|\alpha|^2 : |\beta|^2 = 4 : 1$).

of cooling modules (as shown in Fig. 3a) allows us to implement both the evaporative and recycling strategies. The implementation was guided by following the random-walker diagram shown in Fig. 3b. Specifically, for any event where the photon emerges from the cooling (heating) exit of a cooling module, the random walk position
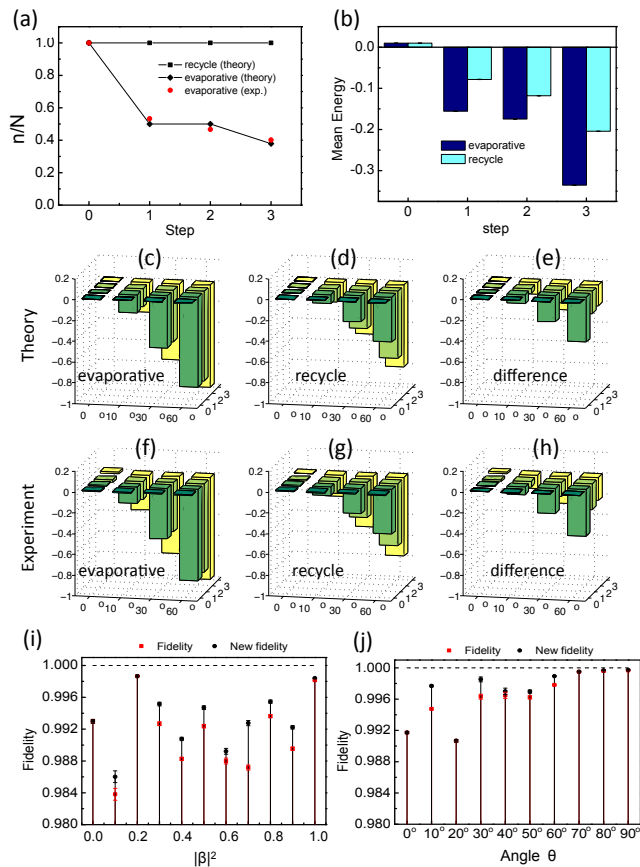
FIG. 5: (Color online). Experimental results. In (a-h) we compare the tradeoff between the evaporative and recycling cooling strategies for Hamiltonian $\sigma_z$, initial state $(|e\rangle + |g\rangle)/\sqrt{2}$, and bias angle $\theta = 10°$. (a) Theory and experiment for the number $n$ of copies obtained out of $N$ initial copies at consecutive steps. The total probability of the recycling algorithm is set to 1, correcting for experimental loses. (b) Experimental results for the corresponding mean energies. (c-e) Theoretical results for the mean energies for the evaporative strategy, the recycling strategy, and their difference. Different bars correspond to different energy bias angles and cooling steps. (f-h) Corresponding experimental predictions. (i) and (j) are the corresponding experimental and revised fidelities. Error bars correspond to the statistical distribution of experimental measurements.

$x$ is increased (decreased) by 1. Across the boundary $x = -1$, for a range of parameters, the walkers have energy $\langle H_s \rangle$ higher than that of the initial state. As in evaporative cooling, separating these hot walkers from the system necessarily lowers the average energy of the system.

The experimental results with multiple steps of the cooling simulation are summarized in Fig. 4. The color-coded energy maps of Fig. 4a correspond to the evaporative strategy. To characterize the efficiency of the cooling method, we considered different initial input states $\alpha|e\rangle + \beta|g\rangle$ for Hamiltonians $H_s = \sigma_z$ and $\sigma_x$, and

different proportions $|\alpha|^2 : |\beta|^2$ between the populations of the ground $|g\rangle$ and excited states $|e\rangle$. We remark that (i) the cooling method does not require the knowledge of the ground states, and (ii) the theoretical values of the mean energy are the same for both Hamiltonians. The first row in each color coded energy map (step 0) represents the mean energy of the initial state. The other rows in an energy map correspond to the mean energy after each step of cooling. The columns of the energy maps correspond to different choices of the energy bias $\theta \equiv \gamma + \pi/2$ (cf. Eq. 2) in the cooling module. For an angle $\theta = 0°$, the mean energy remains constant. For other angle settings ($\theta \neq 0°$), the mean energy decreases with increasing cooling steps. Note that in the evaporative strategy, after the first step, the output states corresponding to heating events ($x = -1$) are discarded. This is reflected in the fact that for all angles $\theta \neq 0°$ the mean energy decreases (output port 0 of the first cooling module). However, at the second step, the random walkers jump to either $x = 0$ and $x = 2$ and no walker is rejected (output ports 00 and 01, see also Fig. 3b). Consequently, the mean energies after the first and second steps are the same (see also Fig. 5a).

We systematically probed the mean energy $\langle H_s \rangle$ and the ground-state probability $P_g = \langle g| \rho_{\exp} |g\rangle$ of the output states corresponding to the cooling events after three steps, Figs. 4b and 4c. The mean energy decreases with increasing ground-state probability $|\beta|^2$ and energy bias $\theta$. The output state approaches the ground state when $\theta$ is close to $90°$, in good agreement with the theoretical prediction. In our experiment, the statistics of each count are considered to follow a Poisson distribution and the error bars are estimated from the standard deviations of the values calculated by the Monte Carlo method. We compared the trade-off between the strategies with and without recycling of "hot" copies. Figures 5(a-h) show the theoretical and experimental results with initial input state $(|e\rangle + |g\rangle)/\sqrt{2}$, Hamiltonian $\sigma_z$, and energy bias angle $\theta = 10°$. It is clear that the mean energy of the evaporative strategy decreases faster than that of the recycling strategy at the cost of a lower total yield. Finally, the experimental fidelities are always larger than 0.983 and the fidelities after post-processing (see methods summary) are even better (compare black vs red data points in Fig. 5i and 5j).

To conclude, our simulation results suggest that cooling for quantum simulation can be experimentally achieved with high fidelity. Due to the modest experimental resource requirement, even the fully scalable version (see [22]) of this method can potentially be implemented with many of the currently available quantum computing architectures, such as trapped ions, superconducting devices and NMR systems. Furthermore, as the solution to classical [28] or quantum [29] computational problems can be encoded in the ground state of certain Hamiltonian, our cooling method can potentially have

applications beyond quantum simulation.

## METHODS

Here we justify the claim in Eq. 1 that for any quantum state $|\psi_{in}\rangle$ that is not an eigenstate of $H_s$, the state $\Lambda_- |\psi_{in}\rangle$ ($\Lambda_+ |\psi_{in}\rangle$), after normalization, has energy $E = \langle H_s \rangle$ lower (higher) than that of $|\psi_{in}\rangle$. To proceed, we performed a eigenvector expansion, which gives $|\psi_{in}\rangle = \sum_k c_k |e_k\rangle$, where $|e_k\rangle$'s are the eigenvectors of $H_s$, i.e., $H_s |e_k\rangle = E_k |e_k\rangle$, and $c_k = \langle e_k |\psi_{in}\rangle$. Consider $\Lambda_\pm |\psi_{in}\rangle = \sum_k c_k \left(1 \pm i e^{-i\phi_k}\right) |e_k\rangle$, where $\phi_k \equiv E_k t - \gamma$. Note that the square norm of the amplitudes are $|c_k|^2 (1 \pm \sin \phi_k)$. It means that apart from an overall constant, each of the weight $|c_k|^2$ of the eigenvectors are scaled by a factor $(1 \pm \sin \phi_k)$. In Fig. 1c, within the range $|\phi_k| < \pi/2$, the function $1 - \sin \phi_k$ is monotonically decreasing. In other words, the lower the eigen-energy is, the higher the weight gains, which results in a lower average energy, i.e., cooling. A similar argument applies for the case of heating.

Here we explain the difference between the "evaporative" strategy and the "recycling" strategy. In implementing the evaporative strategy, we assumed an initial ensemble of identical states (red particles in Fig. 1a). When the random walker position is set to $x = -1$, then the system is rejected, and we restart the experiment with another member in the ensemble. Just like ordinary evaporative cooling, this results in a decrease of overall energy but at a cost of loss of particles (blue particles in Fig. 1a). For the recycling strategy, it is applicable to a single system. We assume the same initial state can be prepared efficiently. When the random walker position is set to $x = -1$, we simply reset the quantum state of the system to the same initial state. For $x \neq 1$, both strategies work in exactly the same way.

The revised fidelities in Fig. 4d and 4e are obtained by mapping each experimental density matrix (obtained using maximum likelihood) to its eigenvector with highest eigenvalue. This corrects isotropic (depolarizing) noise.

### Author Contributions

M.-H.Y. and A.A.-G. are responsible for the main theoretical idea of the cooling method. S.B. performed detailed analysis on the scaling behavior of cooling method. M.-H.Y. drafted the preliminary experimental proposal which was put forwarded by Z.-W.Z. and C.-F.L. The detailed experimental procedures were designed and carried out by J.-S.X., assisted by X.-Y.X. The experiment was supervised by C.-F.L. and G.-C.G. All authors contributed to the writing of the paper and discussed the experimental procedures and results.

## ADDITIONAL INFORMATION

The authors declare no competing financial interests.

————

\* These authors contributed equally to this work.
† Electronic address: cfli@ustc.edu.cn
‡ Electronic address: aspuru@chemistry.harvard.edu

[1] Jordan, S. P., Lee, K. S. M., Preskill, J. Quantum algorithms for quantum field theories, *Science* **336**, 1130-1133 (2012).

[2] Casanova, J., Mezzacapo, A., Lamata, L., Solano, E. Quantum Simulation of Interacting Fermion Lattice Models in Trapped Ions, *Phys. Rev. Lett.* **108**, 190502 (2012).

[3] Kassal, I., Jordan, S. P., Love, P. J., Mohseni, M., Aspuru-Guzik, A. Polynomial-time quantum algorithm for the simulation of chemical dynamics, *Proc. Natl. Acad. Sci. USA* **105**, 18681-18686 (2008).

[4] Baugh, J., Moussa, O., Ryan, C. A, Nayak, A., Laflamme, R. Experimental implementation of heat-bath algorithmic cooling using solid-state nuclear magnetic resonance. *Nature* **438**, 470-473 (2005).

[5] Barreiro, J. T. *et al.*, An open-system quantum simulator with trapped ions, *Nature* **470**, 486-491 (2011).

[6] Zhang, J., Yung, M.-H., Laflamme, R., Aspuru-Guzik, A., Baugh, J. Digital quantum simulation of the statistical mechanics of a frustrated magnet. *Nat. Commun.* **3**, 880 (2012).

[7] Lloyd, S. Universal quantum simulators. *Science* **273**, 1073 (1996).

[8] Buluta, I., Nori, F. Quantum simulators. *Science* **326**, 108 (2009).

[9] Kassal, I., Whitfield, J. D., Perdomo-Ortiz, A., Yung, M.-H., Aspuru-Guzik, A. Simulating chemistry using quantum computers. *Annu. Rev. Phys. Chem.* **62**, 185-207 (2011).

[10] Toyabe, S., Sagawa, T., Ueda, M., Muneyuki, E., Sano, M. Experimental demonstration of information-to-energy

conversion and validation of the generalized Jarzynski equality. *Nature Phys.* **6**, 988-992 (2010).

[11] Osheroff, D. D. Superfluidity in 3He: Discovery and Understanding. *Rev. Mod. Phys.* **69**, 667-682 (1997).

[12] Wieman, C. E., Pritchard, D. E., Wineland, D. J. Atom cooling, trapping, and quantum manipulation. *Rev. Mod. Phys.* **71**, S253-S262 (1999).

[13] Poulin, D., Wocjan, P. Sampling from the Thermal Quantum Gibbs State and Evaluating Partition Functions with a Quantum Computer, *Phys. Rev. Lett.* **103** (2009).

[14] Yung, M.-H., Aspuru-Guzik, A. A quantum-quantum Metropolis algorithm. *Proc. Natl. Acad. Sci. USA* **109**, 754-9 (2012).

[15] Takahashi, S. *et al.* Decoherence in crystals of quantum molecular magnets. *Nature* **476**, 769 (2011).

[16] Boykin, P. O., Mor, T., Roychowdhury, V., Vatan, F., Vrijen, R. Algorithmic cooling and scalable NMR quantum computers. *Proc. Natl. Acad. Sci. USA* **99**, 3388-93 (2002).

[17] Schulman, L., Mor, T., Weinstein, Y. Physical Limits of Heat-Bath Algorithmic Cooling, *Phys. Rev. Lett.* **94**, 120501 (2005).

[18] Kraus, B. *et al.*, Preparation of entangled states by quantum Markov processes, Physical Review A 78, 1-9 (2008).

[19] Verstraete, F., Wolf, M. M., Cirac, J. I. Quantum computation and quantum-state engineering driven by dissipation, *Nat. Phys.* **5**, 633-636 (2009).

[20] DiVincenzo, D. P. The physical implementation of quantum computation. *Fortschr. Phys.* **48**, 771783 (2000).

[21] Weimer, H., Müller, M., Lesanovsky, I., Zoller, P., Büchler, H. P. A Rydberg quantum simulator, *Nat. Phys.* **6**, 382-388 (2010).

[22] See the materials and methods in supplementary information (SI).

[23] Lupascu, A. *et al.* Quantum non-demolition measurement of a superconducting two-level system. *Nature Phys.* **3**, 119-125 (2007).

[24] Aspuru-Guzik, A., Walther, P. Photonic quantum simulators. *Nature Phys.* **8**, 285-291 (2012).

[25] Zhou, X.-Q. *et al.* Adding control to arbitrary unknown quantum operations. *Nat. Commun.* **2**, 413 (2011).

[26] Gao, W.-B. *et al.* Experimental demonstration of a hyper-entangled ten-qubit Schrödinger cat state. *Nature Phys.* **6**, 331-335 (2010).

[27] Lanyon, B. P. *et al.* Simplifying quantum logic using higher-dimensional Hilbert spaces. *Nature Phys.* **5**, 134-140 (2009).

[28] Farhi, E. *et al.* A quantum adiabatic evolution algorithm applied to random instances of an NP-complete problem., *Science* **292**, 4725 (2001).

[29] Feynman, R. Quantum mechanical computers, *Opt. News*, **11**, 1146, (1985).

**SUPPLEMENTARY INFORMATION**

**Demon-like Algorithmic Quantum Cooling and its Realization with Quantum Optics**

Jin-Shi Xu, Man-Hong Yung, Xiao-Ye Xu, Sergio Boixo,
Zheng-Wei Zhou, Chuan-Feng Li, Alán Aspuru-Guzik, Guang-Can Guo

**Contents**

# 1: BASIC PRINCIPLE OF THE SIMULATED COOLING ALGORITHM

Here we explain in detail the basic idea of the cooling algorithm implemented in this experiment. As shown in Fig. 1b, the core of the quantum circuit (cooling module) consists of four components: (a) two Hadamard gates

$$\mathsf{H} \equiv \tfrac{1}{\sqrt{2}} \left( |0\rangle + |1\rangle \right) \langle 0| + \tfrac{1}{\sqrt{2}} \left( |0\rangle - |1\rangle \right) \langle 1| \ , \tag{3}$$

applied to the ancilla qubit in the beginning and at the end of the quantum circuit. (b) a local phase gate,

$$\mathsf{R_z} \left( \gamma \right) \equiv |0\rangle \langle 0| - ie^{i\gamma} |1\rangle \langle 1| \ , \tag{4}$$

where the parameter $\gamma$ plays a role in determining the overall efficiency of the cooling performance of the algorithm. (c) a two-qubit controlled unitary operation,

$$\mathbb{1} \otimes |0\rangle \langle 0| + U \otimes |1\rangle \langle 1| \ , \tag{5}$$

where $\mathbb{1}$ is the identity operator, and

$$U \left( t \right) = e^{-iH_s t} \tag{6}$$

is the time-evolution operator for the system. Here $H_s$ is the Hamiltonian of the system, and the energy is defined as the quantum expectation value of $H_s$. The parameter $t$ also determines the overall efficiency of the algorithm.

For any given initial state (it works equally well for mixed states), $|\psi_{in}\rangle$, the algorithm starts with the product state of the system state $|\psi_{in}\rangle$ and the ancilla state $|0\rangle$,

$$|\psi_{in}\rangle \otimes |0\rangle \ . \tag{7}$$

The quantum circuit then produces the following output state:

$$\frac{1}{2} \left( \mathbb{1} - ie^{i\gamma}U \right) |\psi_{in}\rangle |0\rangle + \frac{1}{2} \left( \mathbb{1} + ie^{i\gamma}U \right) |\psi_{in}\rangle |1\rangle \ . \tag{8}$$

A projective measurement on the ancilla qubit in the computational basis $\{|0\rangle , |1\rangle\}$ yields one of the two (unnormalized) states

$$\left( \mathbb{1} \pm ie^{i\gamma}U \right) |\psi_{in}\rangle , \tag{9}$$

which have mean energies either higher (for outcome $|1\rangle$) or lower (for outcome $|0\rangle$) than that of the initial state $|\psi_{in}\rangle$.

To justify this statement, let us expand the input state in the eigenvector basis $\{|e_k\rangle\}$ of the Hamiltonian $H_s$,

$$|\psi_{in}\rangle = \sum_k c_k |e_k\rangle \ . \tag{10}$$

Note that the vector norms have the following form:

$$\left| \left( \mathbb{1} \pm ie^{i\gamma}U \right) |e_k\rangle \right|^2 = 2 \left( 1 \pm \sin \phi_k \right) \ , \tag{11}$$

where $\phi_k \equiv E_k t - \gamma$ depends on the eigenenergy $E_k$ of $H_s$. In other words, each of the eigenvector weights $|c_k|^2$ is now multiplied by a factor

$$1 \pm \sin \phi_k \tag{12}$$

depending on the measurement result. To simplify our discussion, we will assume that one can always adjust the two parameters, $\gamma$ and $t$, such that

$$-\tfrac{\pi}{2} \leq \phi_k < \tfrac{\pi}{2} \tag{13}$$

for all $k$'s. Then, the factors $(1 - \sin \phi_k)$ are in descending order of the eigenenergies (see Fig. 1c), and the opposite is true for the factors $(1 + \sin \phi_k)$ .

Therefore, apart from an overall normalization constant, the action of the operator $(\mathbb{1} \pm ie^{i\gamma}U)$ is to scale each of the probability weight $|c_k|^2$ by a factor of $(1 \pm \sin \phi_k)$; the probability weights scale to larger values, i.e.,

$$(1 - \sin \phi_k) / (1 - \sin \phi_j) > 1 \tag{14}$$

for the eigenenergy $E_k < E_j$ in the cooling case (i.e., for outcome $|0\rangle$), and vice versa for the heating case (i.e., for outcome $|1\rangle$).

**Comments about the measurement**

The one-bit measurement result of the cooling module correlates with the energy of the state of the simulated system. After the measurement, the state of the system changes. If the state of the system is diagonal in the energy basis, this is strictly a Bayesian update. In general, this is nothing but a (partial) "collapse" of the wave function. If the measurement result is 0, the relative population of the low energy eigenstates of the system increases, Fig. 1(c). That is, if we post-select copies for which the results of a sequence of measurements have a sufficiently higher proportion of zeros than ones, then the average energy decreases, as in evaporative cooling.

When each measurement corresponds to a short time evolution this technique is related to imaginary time evolution, as in diffusion Monte Carlo [?]. If we do not post-select and the system is finite, the relative frequency of zeros and ones will peak on well defined values for different copies of the system. These well defined values are in a one-to-one correspondence with the possible energies of the Hamiltonian. The measurement of the energy can be viewed as a simulation of von Neumann's description of the quantum measurement process: the evolution of the system with Hamiltonian $H$ couples with the position of a "measuring pointer." The pointer, in our case, is a binary ancilla qubit.

**Comments about "cooling"**

With our method, we do not result directly with a thermal state with Boltzmann distribution. Therefore, temperature is not well-defined. However, the entropy associated with the diagonal elements in the energy basis can be properly defined. Our method allows us to reduce the average energy and also the entropy. Of course, it is also possible to combine our method with other existing methods to project the exact thermal states, which will also allow us to define temperature.

For example, if we start with the identity matrix $I$ as our initial state, we can consider it as an infinite-temperature state. When we simulate a small time evolution and zero $\gamma$, then the scaling factor (e.g. see Fig. 1) becomes approximately the same as the Boltzmann factor

$$1 - \sin \phi_k \approx e^{-E_k t} \quad . \tag{15}$$

To further improve the fidelity, one may apply the projection method described in Ref. [? ? ]. We can repeat the same procedure to reach states with a lower temperature.

**Requirement for a fully scalable implementation**

In our experiment, we demonstrated a proof-of-principle experiment for implementing our cooling algorithm. However, the experimental setup is specifically designed for cooling the polarization degrees of freedom. Here we discuss the requirements for a fully scalable implementation. First of all, we need a supply of fresh ancilla qubits prepared in the $|0\rangle$ state. It is not strictly required to have perfect $|0\rangle$ ancilla, but an error would decrease the cooling efficiency. Alternatively, if we are able to reset the ancilla qubit quickly, we can also employ only one ancilla qubit through out. Secondly, we will need to be able to maintain the coherence of the system qubits. Therefore, we expect error corrections will still be required, unless we can finish the cooling within the coherence time of the system. Thirdly, we will also need to have fast projective measurement on the ancilla qubits, which will allow us to be able to implement our feedback control system. An example is shown in Fig. 6. These requirements are not much different from those required for implementing a typical quantum algorithm. The main feature of this cooling algorithm is the modest requirement of using ancilla qubits, which could reduce the resources for expanding it into a fault-tolerant structure.

## 2. SCALING ANALYSIS OF THE SIMULATED COOLING ALGORITHM

**Simplified model**

We study the complexity of preparing the ground state for easy of comparison with other methods. We focus on Hamiltonians with only two different energies. The generalization of the same problem to systems with more energies is straightforward. The degeneracy of the energy levels turns out not to be of any consequence for the resulting cost, only the projection probability on the lowest energy subspace is important. With that in mind, we will write the equations for a two level system to simplify the notation.
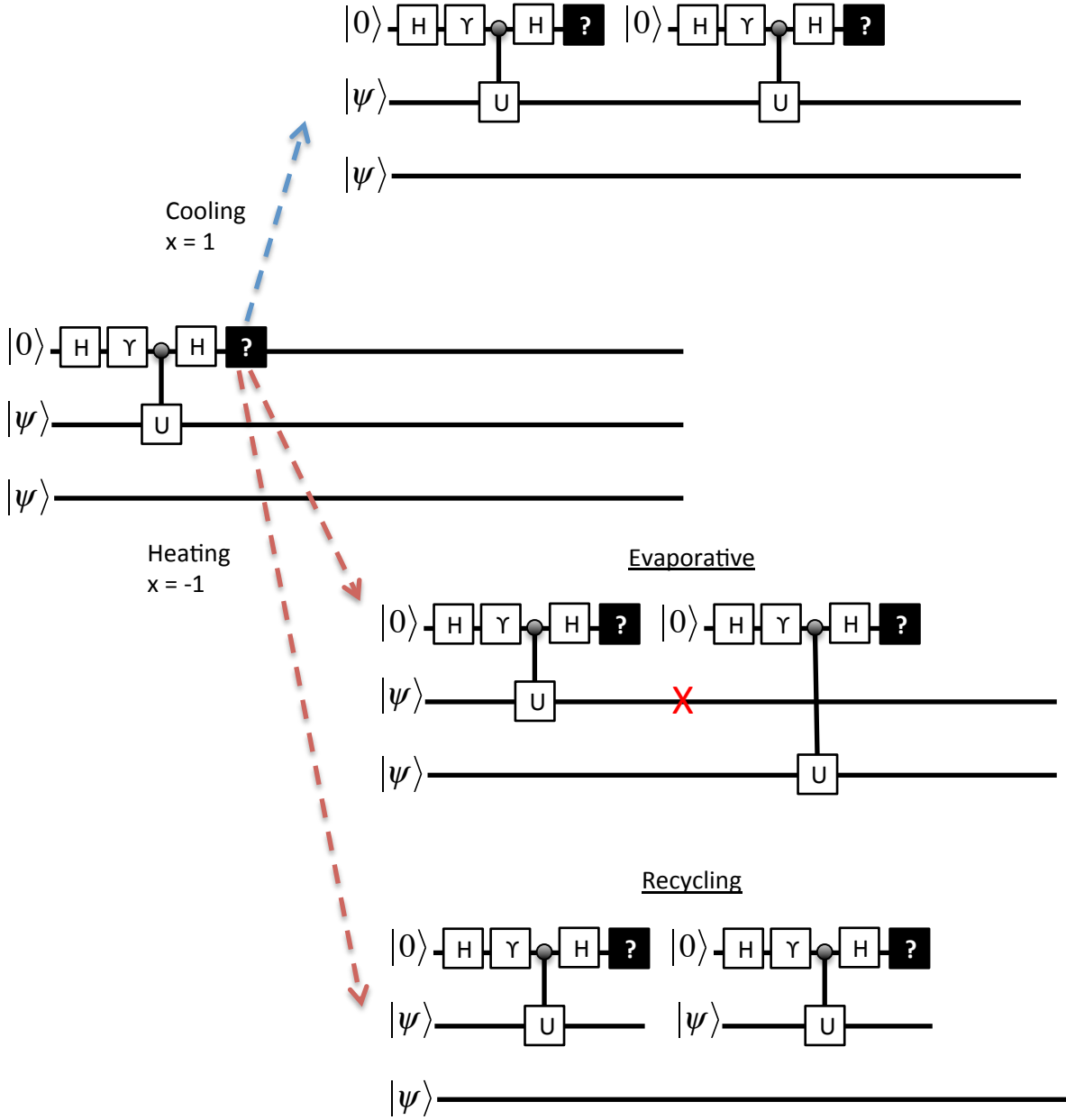
FIG. 6: An example of the scalable implementation of the quantum cooling algorithm. When the first step of cooling is implemented, a projective measurement (labeled by a question mark "?") is performed on the first ancilla qubit. The measurement result then determines if the second ancilla would interact with the first system or the second system. If cooling is resulted, then $x = 1$, and the same quantum circuit is applied to the same quantum system. It is same for both evaporative strategy and recycling strategy. However, if the measurement outcome is heating, then for the evaporative strategy, the system is rejected, and a new member is employed. For the recycling strategy, the same system is reset and sent to the same quantum circuit.

We denote the two energy eigenstates by $|e_0\rangle$ and $|e_1\rangle$ with energies $E_0$ and $E_1$, and define

$$|\psi_{in}\rangle = \sqrt{p}\,|e_0\rangle + \sqrt{1-p}\,|e_1\rangle \quad . \tag{16}$$

Let us ignore for the moment the possibility of filtering high energy states after too many "heating" measurements. The insight gained with this assumption can be applied to the more sophisticated algorithms in the text. We can then also assume, without loss of generality, that all the measurements are done together at the end of the computation. Therefore, if there are a total of $k$ steps, we get the state (prior to the final measurement)

$$\sum_{j=0}^{k} \sqrt{\binom{k}{j}} \left( \sqrt{p(1/2+a)^{k-j}(1/2-a)^j} |e_0\rangle |\mathcal{X}_j\rangle + \sqrt{(1-p)(1/2+b)^{k-j}(1/2-b)^j} |e_1\rangle |\mathcal{Y}_j\rangle \right) ,$$

where $|\mathcal{X}_j\rangle$ and $|\mathcal{Y}_j\rangle$ are properly normalized states,

$$a = \frac{1}{2}\sin(E_0 t - \gamma) \quad , \quad b = \frac{1}{2}\sin(E_1 t - \gamma) \quad , \tag{17}$$

and $j$ denotes the numbers of 0's in both $|\mathcal{X}_j\rangle$ and $|\mathcal{Y}_j\rangle$. The parameter $\gamma$ is a controllable energy bias, see Fig. 1 in the main text.

The probability to get $j$ zeros on the final measurements of the ancillae is

$$p\binom{k}{j}(1/2+a)^{k-j}(1/2-a)^j + (1-p)\binom{k}{j}(1/2+b)^{k-j}(1/2-b)^j .$$

This is a mixture (with mixing probability $p$) of two binomial distributions. The left side binomial (corresponding to the ground state) concentrates on the interval

$$k\left( \left(\frac{1}{2}-a\right) \pm \frac{1}{\sqrt{k}}\sqrt{\frac{1}{4}-a^2} \right) \tag{18}$$

and the right side binomial concentrates on the interval

$$k\left( \left(\frac{1}{2}-b\right) \pm \frac{1}{\sqrt{k}}\sqrt{\frac{1}{4}-b^2} \right) . \tag{19}$$

The first binomial corresponds to the probability of finding the ground state in the post-condition state after getting $j$ zeros. Because we want to prepare the ground state, the binomials should have little intersection. This happens when

$$k\left( \left(\frac{1}{2}-b\right) + \frac{1}{\sqrt{k}}\sqrt{\frac{1}{4}-b^2} \right) \ll k\left( \left(\frac{1}{2}-a\right) - \frac{1}{\sqrt{k}}\sqrt{\frac{1}{4}-a^2} \right) .$$

This is equivalent to

$$\sqrt{k}(b-a) \gg \frac{1}{2} - (a^2 + b^2) . \tag{20}$$

The most relevant case is when the energies and the bias are small. We can do an expansion in terms of the small parameter $\Delta t$, where $\Delta$ is the gap and $t$ is the evolution time. The parameters $a$ and $b$ are then small, $\mathcal{O}(\Delta t)$, using big-O notation. We get

$$\frac{1}{2} - (a^2 + b^2) = \frac{1}{2} + \mathcal{O}((\Delta t)^2) \tag{21}$$

$$b - a = \frac{\Delta t}{2} + \mathcal{O}((\Delta t)^2) . \tag{22}$$

This gives the expected result

$$\sqrt{k} \gg \frac{1}{\Delta t} . \tag{23}$$

That is, the number of measurements necessary to prepare the ground states has an scaling

$$k \in \mathcal{O}((\Delta t)^{-2}) . \tag{24}$$

If the binomials are separated, when we measure we get a number of zeros

$$j \sim k(1/2 - b) \quad , \tag{25}$$

which happens with probability $1 - p$, and then we have collapsed on $|e_1\rangle$, or we get a number of

$$j \sim k(1/2 - a) \quad , \tag{26}$$

which happens with probability $p$, and then we have collapsed on $|e_0\rangle$. The number of measurements necessary to prepare the ground state scales like

$$\frac{1}{p(\Delta t)^2} \quad . \tag{27}$$

### Monte Carlo simulations

We performed Monte Carlo simulations to test the scalings explained above for better algorithms, such as those implemented in the experiment. Notice that in the previous subsection we obtained scalings for the case when all the measurements are performed at the end or, equivalently, measurements are taken at each step but the result of the measurement is not taken into account at subsequent steps. Nevertheless, in the experiment adaptive action was taken taking into account the results of previous measurements (absorption and reflection boundaries, explained in main text). The intuition is that even an optimal adaptive action does not change the fundamental scaling. This is what we saw with Monte Carlo simulations.

The actual experiment implemented an algorithm that keeps track of the difference $x$ between the number of measurement results equal to 0 and those equal to 1 in the ancilla,

$$x = \#0 - \#1 \quad . \tag{28}$$

The algorithm implemented in the experiment obeys two boundary conditions:

1. If the number of measurement results equal to 0 is less than the number of 1's ($x \leq 0$), we reinitialize with the initial state. This is a "reflective" boundary condition.

2. For some predefined constant $c_{\text{abs}}$, if $x = c_{\text{abs}}$ then stop. This is an "absorbing" boundary condition.

In addition, we need to define a constant $c_{\text{bound}}$ such that we stop after reaching this number of steps. This is because this simple method can collapse to the excited state and never reach the absorbing wall (see previous subsection).

We can analyze this algorithm following the intuition gained from the non-adaptive case explained above. Because we are interested in the asymptotic case with small energy differences, we set the energy bias

$$\gamma = 0 \quad . \tag{29}$$

The position $x$ of the random walker without boundary conditions was found to be distributed as a mixture of two (displaced) binomials distributions, centered around

$$\sin(Et) * k \tag{30}$$

with $E$ taking the values of the ground and excited state energies, $k$ the total number of measurements, and $t$ is the evolution time.

For the constant $c_{\text{bound}}$ we can use our prediction on the number of steps needed to cool optimally

$$c_1 \frac{1}{(\Delta t)^2} \frac{1}{p} \quad , \tag{31}$$

with a constant $c_1$ that depends on the details of the algorithm. We want to show that this scaling holds for significant changes in $\Delta t$ and $p$, when this parameters have small values. Because our process is not optimal, we actually use

$$c_{\text{bound}} = 3 * \text{pred} \tag{32}$$

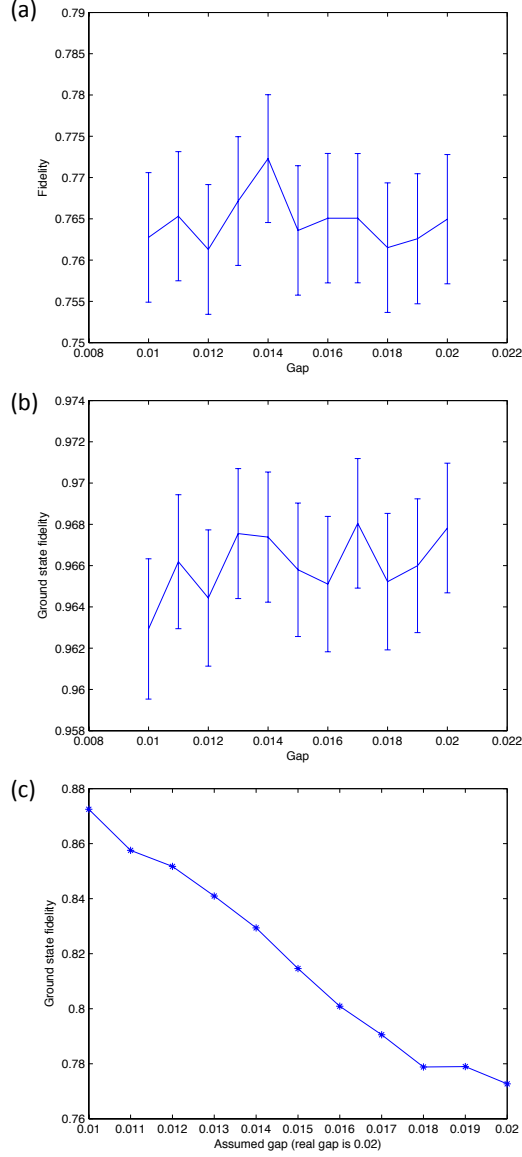$$\text{pred} = c_1 \frac{1}{\Delta^2 p} \quad , \tag{33}$$

FIG. 7: (a) Final fidelity for the ground state for the values explained in the text. (b) Final fidelity for the ground states for the values explained in the text when trowing away states that reach $c_{\mathrm{bound}}$ measurements. (c) Fidelity changes if we choose the reflective and absorbing boundary conditions according to the equations in the text, but using assumed gap values that do not corresponding to the real gap. The gap was kept at 0.02, but the gap used for the boundary conditions was the one indicated in the $x$-axis.

where we use the constant $c_1 \sim 2.7$ from the numerics of the optimal filtering algorithm (see below). Although in principle one can only use estimates of the gap $\Delta$ and the initial population $p$, we assume that this estimates are indeed good, and use the exact values in our numerics. Furthermore, we set the ground state energy $E_0 = -\Delta$ and the excited state energy $E_1 = 0$. These choices do not affect the fundamental scaling.

Finally, we choose a value for the absorption boundary condition. We want this to be a value for $x$ where states already have a good overlap with the ground state. We simply use the predicted average after the predicted number of measurements necessary to collapse

$$c_{\mathrm{abs}} = \mathrm{pred} * \sin(E_0 t) . \tag{34}$$

We performed Monte-Carlo numerics for $p = 0.2$ and $\Delta t$ between 0.01 and 0.02, Fig. 7. For these values, the number of maximum measurements ($c_{\mathrm{bound}}$) goes between 400000 and 100000, and the positions of the absorbing boundary condition goes between 1350 and 675. Nevertheless, the final fidelity with the ground state is quite constant, a clear

indication that we understand the scaling correctly. The fidelity is always close to 0.76. For the error bars we use the expression

$$\hat{\mu} \pm 1.96 \frac{\hat{\sigma}}{100} \ , \tag{35}$$

where $\hat{\sigma}$ is the sample standard deviation, $\hat{\mu}$ is the sample average, and we divide by the square root of the number of samples, $\sqrt{10000}$.

As a simple improvement, we can remove from the calculation of the fidelity the states that reach the maximum number of steps, $c_{\mathrm{bound}}$. This corresponds to simply restarting again with an initial state. With the values chosen, only 20% of the measurement histories arrive to $c_{\mathrm{bound}}$, so the probability of cooling with this method is also high. Further, the probability to always arrive at $c_{\mathrm{bound}}$ decreases exponentially in the number of trials. The corresponding fidelities are depicted in Fig. 7.

We also check that the fidelity does indeed vary substantially if we keep the gap fixed but change the reflective and absorbing bound conditions. This is plotted in Fig. 7. For these numerics the gap was kept constant at 0.02, but the reflective and absorbing boundary conditions were chosen as if the gap was different (between 0.01 and 0.02, as before).

We also tested that the same fundamental scaling holds for an optimal refreshing schedule. The optimal refreshing schedule for the two level system is this: replace the current state with the initial state whenever the temperature of the current state is higher than the temperature of the initial state. This can be calculated with linear cost in the number of steps assuming that the energies of the ground state and the excited states are known, as well as the initial population of the ground state. In this case the boundary conditions and the bound on the maximum number of steps are unnecessary. Nevertheless, the distribution of the number of steps was found to be given by Eq. (31). The value of the constant $c_1$ was found by fitting the Monte Carlo sampling data.

## Summary

In summary, we focus on the complexity of preparing the ground state. The scaling is expressed in terms of the energy gap $\Delta$ between the ground state and the first excited state, the evolution time $t$ of the simulated Hamiltonian for the weak energy measurement, and the population (probability) $p$ of the ground state. The basic scaling is inversely proportional to $(\Delta t)^2 p$. If possible, the theoretical optimal scaling occurs when $t \sim 1/\Delta$, giving single-ancilla quantum phase estimation. Longer evolution times for each measurement require longer coherent times for the ancillae. It is also worth noting that the post-conditioned distribution is different for different evolution times and energy biases, which might be advantageous in some situations. Finally, in theory, the scaling with $p$ can be improved to $\sqrt{p}$ using amplitude amplification . This comes at the expense of many more quantum operations, and therefore is less practical than the approach proposed here.

## 3. FROM QUANTUM CIRCUIT TO EXPERIMENTAL IMPLEMENTATION

In this section, we describe the experimental implementation of the quantum circuit for the cooling module in Fig. 1. We will focus on a single cooling module, and the cooling with respect to the Hamiltonian $\sigma_z$. The $\sigma_x$ Hamiltonian is achieved by a rotation of the basis. Here we reproduce the relevant parts of the figures in the main text in Fig. 8. The goal here is to explain how to achieve a unitary transformation that is equivalent to the one in the quantum circuit shown in Fig. 8a. Our strategy is not to implement each operation separately, but to construct an effective transformation that produces the same overall result as the quantum circuit.

### Specification of certain simulation details

1. In our experiment, for the Hamiltonian $\sigma_z$, the mapping of the excited $|e\rangle$ and ground state $|g\rangle$ is $|e\rangle = |H\rangle$ and $|g\rangle = |V\rangle$, where $|H\rangle$ and $|V\rangle$ represent the horizontal and vertical polarization states of a single photon, respectively. For the $\sigma_x$ Hamiltonian the excited state is $|e\rangle = (|H\rangle + |V\rangle)/\sqrt{2}$ and the ground state is $|g\rangle = (|H\rangle - |V\rangle)/\sqrt{2}$.

2. For the $\sigma_z$ Hamiltonian, the polarization state of the photon is mapped to the logical state of the system as $|0\rangle = |H\rangle$ and $|1\rangle = |V\rangle$. The two different path of the interferometer serves as the logical qubit of the ancilla.
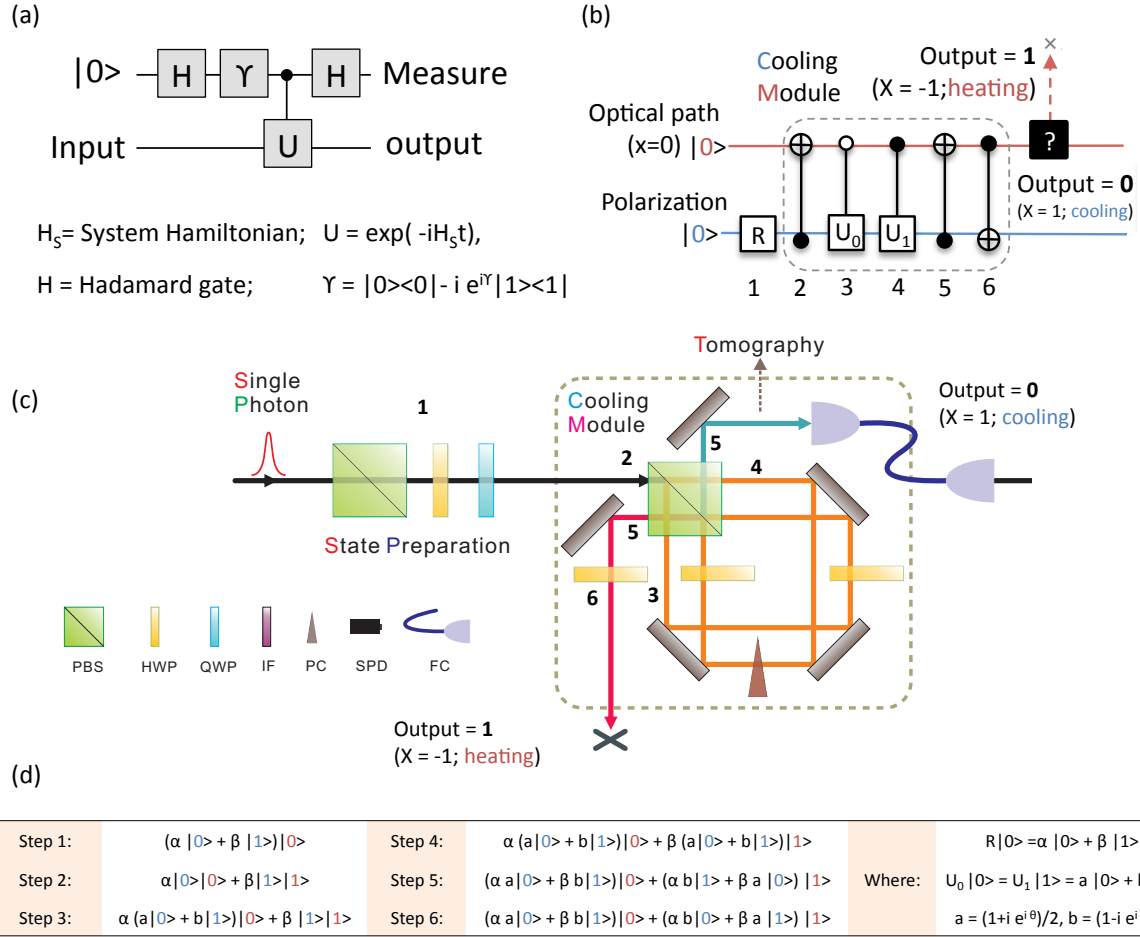
FIG. 8: (Color online). The conversion from the quantum circuit to the experimental implementation. The abbreviations refers to polarization beam splitter (PBS), half-wave plate (HWP), quarter-wave plate (QWP), interference filter (IF), quartz plate compensator (PC), single photon detector (SPD), and fiber connector (FC). See the text for the explanation of the transformations.

The system is prepared in the state $\alpha|0\rangle + \beta|1\rangle$ (blue basis, see Fig 3d) and the ancilla qubit is prepared as $|0\rangle$ (red basis) (step 1).

3. In order to simulate cooling with the Hamiltonian $\sigma_x$, the $\sigma_x$ transform was applied to the input and output ports: we rotate the basis from $|H\rangle$ and $|V\rangle$ to $1/\sqrt{2}(|H\rangle+|V\rangle)$ and $1/\sqrt{2}(|H\rangle-|V\rangle)$ This transform consists of a half-wave plate (HWP) with the angle setting at 22.5° and a tiltable quarter-wave plate (QWP). The logical circuit corresponding to the experimental setup is shown in Fig. 3(c), and the corresponding sequence of states is shown in Fig. 3(d).

4. The input photon pulses for the simulation were generated by a laser with a central wavelength of 800 nm and a repetition rate of 76 MHz, attenuated to the single photon level.

5. The measurement bases for the tomography were set by a QWP, a HWP and a polarization beam splitter (PBS). The photon was finally detected by a single photon detector (SPD) equipped with a 3 nm interference filter (IF). The probability of each output can be directly deduced from the single photon counts of the tomography measurements.

**Step-by-step instruction of the implementation of the cooling module**

1. In our setup, a photon is generated from the single photon source shown in Fig. 8c.

2. The photon is then passed through the state preparation module consisting of a polarization beam splitter (PBS), half-wave plate (HWP) and a quarter-wave plate (QWP). The resulting state is denoted as $\alpha|0\rangle + \beta|1\rangle$ (blue basis, see Fig 8d). The state associated with the path degrees of freedom is denoted as $|0\rangle$. Combining the two, we have the state

$$(\alpha\,|0\rangle + \beta\,|1\rangle)\,|0\rangle \tag{36}$$

   as the input state for the cooling module. This corresponds to step 1 of Fig. 8.

3. The incident photon is then split by a polarization beam splitter, the horizontal polarized photons propagate directly while the vertical polarized photons reflect. This can be considered as a controlled-NOT operation. The resulting state becomes

$$\alpha\,|0\rangle\,|0\rangle + \beta\,|1\rangle\,|1\rangle \quad . \tag{37}$$

   This corresponds to step 2 of Fig. 8.

4. For each path, a unitary operation is realized by using two half-wave plates (HWP), and a quartz plate compensator (PC). The resulting state is

$$\alpha\,(a\,|0\rangle + b\,|1\rangle)\,|0\rangle + \beta\,(a\,|0\rangle + b\,|1\rangle)\,|1\rangle \quad . \tag{38}$$

   This corresponds to step 3 and step 4 in Fig. 8.

5. The two paths are then recombined on the same polarization beam splitter (PBS). The same controlled-NOT is applied, and the resulting is

$$(\alpha a\,|0\rangle + \beta b\,|1\rangle)\,|0\rangle + (\alpha b\,|1\rangle + \beta a\,|0\rangle)\,|1\rangle \quad . \tag{39}$$

   This corresponds to step 5 in Fig. 8.

6. For the path $|1\rangle$, a half-wave plate (controlled-not gate) is applied to the polarization state, giving the final state

$$(\alpha a|0\rangle + \beta b|1\rangle)|0\rangle + (\alpha b|0\rangle + \beta a|1\rangle)|1\rangle \quad . \tag{40}$$

   Note that the unitaries are $U_0|0\rangle = U_1|1\rangle = a|0\rangle + b|1\rangle$, where $a = (1 + ie^{i\theta})/2$ and $b = (1 - ie^{i\theta})/2$. This corresponds to step 6 in Fig. 8.

7. At one output port, denoted as 0, the photon state is cooled and was sent to the next cooling module. At the other output port, denoted by 1, the photon is heated and was either rejected or recycled (re-prepared to the initial state and sent to the next cooling module).

## 4. ADDITIONAL EXPERIMENTAL RESULTS

Figure 9 shows the experimental results for the state transformation carried out by a single cooling module which simulates the Hamiltonian

$$H_s = \sigma_z \,. \tag{41}$$

The output state (photon) at the output port 1 (which corresponds to heating) is rejected. The ratio between $|e\rangle$ and $|g\rangle$ of the output state decreases by a factor

$$(1 - \sin\theta)/(1 + \sin\theta) \,. \tag{42}$$

As a result, the output state becomes closer to the ground state with increasing $\theta$, which is verified by our experimental results. For an energy bias angle $\theta = 0°$ the state simply rotates in the equatorial plane of the Bloch sphere. For the input state

$$(|e\rangle + |g\rangle)/\sqrt{2} \,, \tag{43}$$

the output state as a function of the energy bias angle $\theta$ has Bloch sphere angles

$$\langle \sigma_y \rangle = \cos\theta \quad \text{and} \quad \langle \sigma_z \rangle = -\sin\theta \,. \tag{44}$$

Figure 9a shows the mean energies and ground state probabilities for different initial states (organized in panels with different colors) and different energy bias angles. The fidelities of the reconstructed states are shown in Fig. 9b. Red squares represent the experimental results and black dots represent the revised fidelities (see Methods Summary). The fidelities of the final states are larger than 0.978. Due to the compensation of symmetry noise, the revised fidelities are larger.

Figure 10 shows the experimental results with evaporative and recycling strategies with initial input states

$$\left(1/\sqrt{5}\right)|e\rangle + \left(2/\sqrt{5}\right)|g\rangle \quad \text{and} \quad \left(2/\sqrt{5}\right)|e\rangle + \left(1/\sqrt{5}\right)|g\rangle \tag{45}$$

respectively for the left and right panel, for Hamiltonian $\sigma_z$ (see also Fig. 4(f-m)). Figure 10(a) depicts the success probabilities at each step with evaporative and recycling strategies for input state $(1/\sqrt{5})|e\rangle + (2/\sqrt{5})|g\rangle$ ($\theta = 10°$).



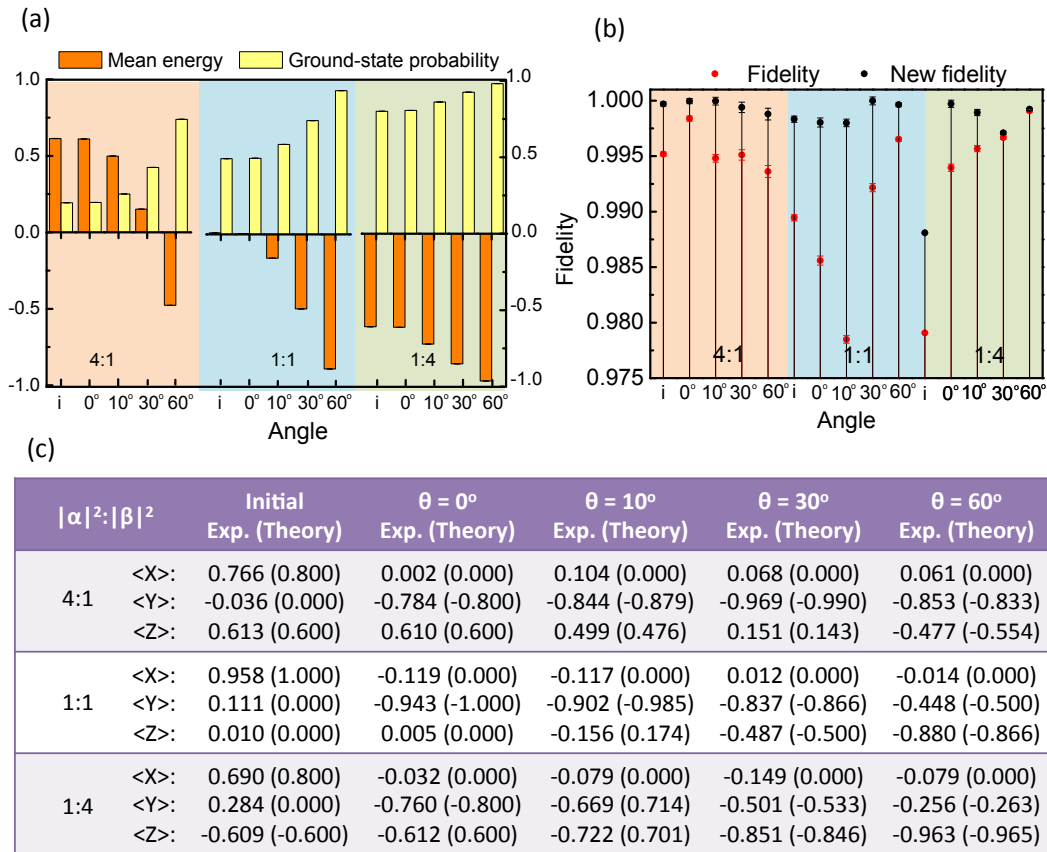| $\|\alpha\|^2 : \|\beta\|^2$ | | Initial<br>Exp. (Theory) | $\theta = 0°$<br>Exp. (Theory) | $\theta = 10°$<br>Exp. (Theory) | $\theta = 30°$<br>Exp. (Theory) | $\theta = 60°$<br>Exp. (Theory) |
|---|---|---|---|---|---|---|
| 4:1 | \<X\>: | 0.766 (0.800) | 0.002 (0.000) | 0.104 (0.000) | 0.068 (0.000) | 0.061 (0.000) |
| | \<Y\>: | -0.036 (0.000) | -0.784 (-0.800) | -0.844 (-0.879) | -0.969 (-0.990) | -0.853 (-0.833) |
| | \<Z\>: | 0.613 (0.600) | 0.610 (0.600) | 0.499 (0.476) | 0.151 (0.143) | -0.477 (-0.554) |
| 1:1 | \<X\>: | 0.958 (1.000) | -0.119 (0.000) | -0.117 (0.000) | 0.012 (0.000) | -0.014 (0.000) |
| | \<Y\>: | 0.111 (0.000) | -0.943 (-1.000) | -0.902 (-0.985) | -0.837 (-0.866) | -0.448 (-0.500) |
| | \<Z\>: | 0.010 (0.000) | 0.005 (0.000) | -0.156 (0.174) | -0.487 (-0.500) | -0.880 (-0.866) |
| 1:4 | \<X\>: | 0.690 (0.800) | -0.032 (0.000) | -0.079 (0.000) | -0.149 (0.000) | -0.079 (0.000) |
| | \<Y\>: | 0.284 (0.000) | -0.760 (-0.800) | -0.669 (0.714) | -0.501 (-0.533) | -0.256 (-0.263) |
| | \<Z\>: | -0.609 (-0.600) | -0.612 (0.600) | -0.722 (0.701) | -0.851 (-0.846) | -0.963 (-0.965) |

FIG. 9: (Color online). Experimental results for a single cooling module with initial state $(|e\rangle + |g\rangle)/\sqrt{2}$ as a function of the energy bias angle $\theta$. (a) Mean energies and ground-state probabilities of the reconstructed states for different energy bias angles. Different color panes represent the cases with different initial input states ("i" $= \alpha|e\rangle + \beta|g\rangle$) with relative populations $|\alpha|^2 : |\beta|^2 = 4:1, 1:1, 1:4$. (b) The fidelities of the reconstructed states. Red squares represent the experimental fidelities. Black dots represent revised fidelities. Error bars are the corresponding standard deviations. (c) Tomography data.
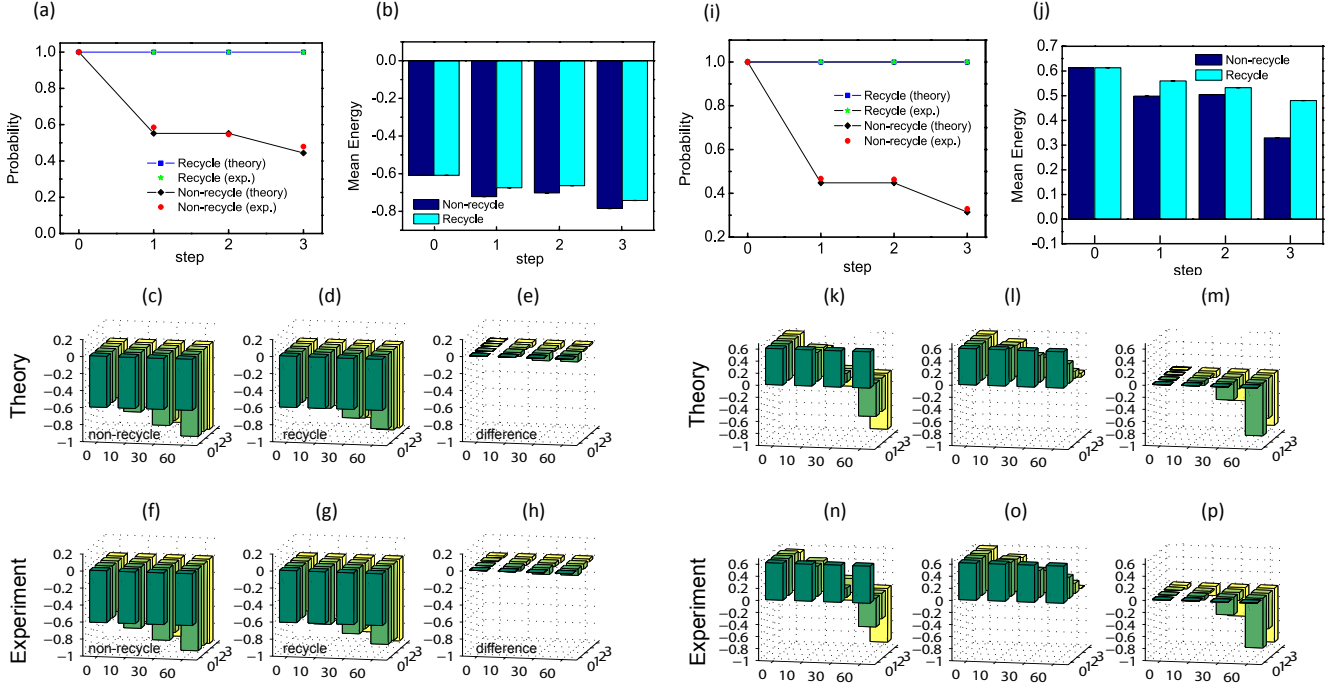
FIG. 10: (Color online). Comparison of simulated cooling with evaporative and recycling strategies for the input states $(1/\sqrt{5})|e\rangle + (2/\sqrt{5})|g\rangle$ (left) and $(2/\sqrt{5})|e\rangle + (1/\sqrt{5})|g\rangle$ (right) for Hamiltonian $\sigma_z$. (a) Experimental results for the success probabilities in each cooling step with evaporative and recycling strategies for input state $(1/\sqrt{5})|e\rangle + (2/\sqrt{5})|g\rangle$ (and $\theta = 10°$). (b) Experimental results for the corresponding mean energies. (c-e) theoretical results for the mean energies for the evaporative strategy, the recycling strategy, and their difference. (f-h) Corresponding experimental results. Figures (i-p) show the same data but now with input state $(2/\sqrt{5})|e\rangle + (1/\sqrt{5})|g\rangle$.

Figure 10(b) shows the mean energies with evaporative and recycling strategies. Figures 10(c-e) indicate the theoretical predictions for the mean energies for the cases with evaporative, with recycling, and their difference. Figures 10(f-h) are the corresponding experimental results. The difference between the cases with evaporative and recycling is small compared to the case of Fig. 4. Figure 10(i-p) shows the exact same plots for the input state $(2/\sqrt{5})|e\rangle + (1/\sqrt{5})|g\rangle$. The difference between the cases with evaporative and recycling is larger than that in Fig. 10(c-h), as shown in Fig. 10(k-p).

In the experiment, we performed three steps of cooling, we show the theoretical calculation for up to ten cooling steps in Fig. 11. The mean energies with evaporative are always smaller than the case with recycling.
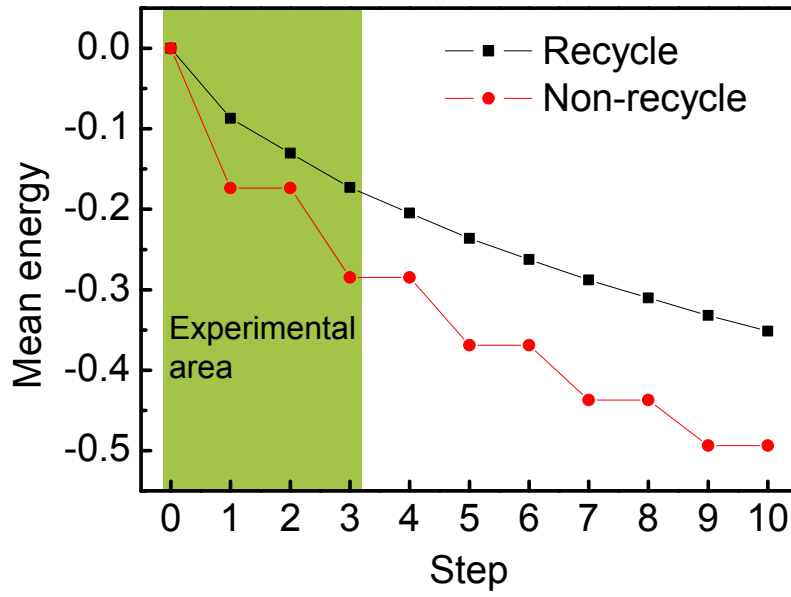
FIG. 11: (Color online). Theoretical results for the mean energies with ten cooling steps and Hamiltonian $\sigma_z$ . Black squares represent the results with recycling and the red dots represent the case with evaporative. The initial state is $(|e\rangle + |g\rangle)/\sqrt{2}$ and the energy bias angle $\theta$ is set to $10°$.